A Appendices

A.1 Exponential moving average

We compute the network's neuronal instantaneous spike rates as exponential moving averages (EMAs), which accumulate spikes over time (see Eq. 9). EMAs are utilized to track recent neuronal activity levels. Concurrently, lifetime average values are also calculated using EMAs, which are crucial for maintaining homeostatic stability. This method helps stabilize the neural network by adjusting neuronal properties or synaptic strengths to sustain consistent activity levels over time.

$$x_j(t) = (1 - \zeta)x_j(t-1) + \zeta \cdot z_j(t), \tag{9}$$

where $\zeta = 1 - e^{-\frac{1}{10}}$, indicating that the 10 ms is a temporal window of the moving average weighted with exponential decay. The initialization of x_j is 0. The exponential moving average is calculated dynamically and updated along with synaptic weights.

$$\langle x_j \rangle := (1 - \xi) \cdot \langle x_j \rangle + \xi \cdot \overline{x}_j, \tag{10}$$

where $\xi = 1 - e^{-1}$. It is dynamically updated to ensure the sum of the weights remains constant over time.

A.2 Detailed parameters and connectivity settings for the model

Detailed neural dynamics: The feed-forward connection, labeled $\text{FF}_{ij}^{(\text{image}\to\text{E})}$, links pixel X_j of the whitened image patch to excitatory (E-) neuron i. $W_{ij}^{(\text{K}^*\to\text{K})}$ signifies the synaptic weight from neuron j of neuron class K^* to neuron i of neuron class K, with its sign determined by the connection type, described as $\beta_{ij}^{(\text{K}^*\to\text{K})}$ (the neuron receives E-connections, set as +1; conversely, the neuron receives inhibitory (I-) connections, the sign is set as -1). $z_j^{(\text{K}^*)}(t)$ indicates the spike output of neuron j at time t. Upon reaching the spike threshold θ (initialized as 2), a spike is emitted, $z_j^{(\text{K}^*)}(t)$ is set to 1, then the membrane potential is reset to 0 mV, remaining so until the refractory period (3 ms) concludes. Within primary visual cortex (V1), homeostatic plasticity [34, 55] ensures neural activity stability by dynamically adjusting the firing threshold θ. This adjustment is based on the deviation of the current firing rate $p_i(t)$ from the target rates $p_i^{(\text{K})}$ ($p^{(\text{E})} = 2$, $p^{(\text{I})} = 4$), as outlined in Eq. 6 [55]. We assign $\tau^{(\text{E})} = 10$ ms for E-neurons and $\tau^{(\text{I})} = 5$ ms for I-neurons. To enhance computational efficiency, we set the time step to 1 ms.

Hyperparameters: For the synaptic plasticity, learning rates are $\eta_{\text{FF}} = 0.2$ (image to E-neurons), $\eta_{\text{EE}} = 0.01$ (E- to E-neurons), $\eta_{\text{EI}} = 0.7$ (I- to E-neurons), $\eta_{\text{II}} = 1.5$ (I- to I-neurons), and $\eta_{\text{IE}} = 0.7$ (E- to I-neurons), while the neural connectivity parameters are $\alpha_{\text{max,E}} = 1.0$ (E- max weight), $\alpha_{\text{max,I}} = 0.5$ (I- max weight), $\sigma_{\text{EE}} = 3.5$ (E-E coupling range), $\sigma_{\text{EI}} = 2.9$ (E-I coupling range), $\sigma_{\text{IE}} = 2.6$ (I-E coupling range), and $\sigma_{\text{II}} = 2.1$ (I-I coupling range).

Neural connectivity within 2D cortical area: E- and I- neurons are arranged symmetrically on a two-dimensional lattice, as illustrated in Fig. 5b. Periodic boundary conditions are employed to mimic the large number of neurons in the actual V1 cortical surface. Specifically, neurons at the boundary are connected to neurons at corresponding symmetric positions on the opposite boundary. The initial connection weights between neurons are modeled by a Gaussian function of their distance (see Fig. 5c), which can be expressed as:

$$W_0^{\text{K}^*\to\text{K}}(i,j) = \alpha_{\text{K}^*} \times \exp\left(\frac{-d(i,j)^2}{2\sigma_{\text{K}^*}{}^2}\right). \tag{11}$$

In this equation, $d(i,j)$ represents the Euclidean distance from neuron i to neuron j in a grid, α determines the maximum connection weight, which is set to $\alpha_{\text{EE}} = 1$, $\alpha_{\text{EI}} = 1$, $\alpha_{\text{IE}} = 0.5$, $\alpha_{\text{II}} = 0.5$, and σ governs the rate at which the weight decays with distance. The synaptic types predominantly determine the parameters for this connection weight distribution function. To accurately replicate the neuronal architecture of V1 in macaques. The connectivity radiuses, denoted by σ, are set to $\sigma_{\text{EE}} = 3.5$, $\sigma_{\text{EI}} = 2.9$, $\sigma_{\text{IE}} = 2.6$, $\sigma_{\text{II}} = 2.1$. These values are based on anatomical data indicating that the axon length scales of E- and I-neurons are approximately 200 μm and 100 μm, respectively, while the dendrite length scales are around 150 μm for E-neurons and 75 μm for I-neurons in the V1 [62, 63, 64]. We prune any connection strengths below a threshold of 0.01 to maintain computational efficiency and biological plausibility.

16

A.3 Anatomical data integration

Neural connection data

The experimental subjects include six adult cats with unknown genders, with data sourced from research by Armen Stepanyants et al.[63]; and eight macaques, aged 5-11 years, including six males and two females, with data sourced from research by Joseph Amatrudo et al.[64].

Neuronal synaptic plasticity

The subjects are rats aged 14-16 days, with unknown gender and quantity, with data sourced from research by Holmgren et al.[57]; transgenic mice, with unknown quantity and gender, with data sourced from research by Hofer et al. [47].

Retinal-V1 topological projection data

Receptive field (RF) data: V1 neuron counts for macaques, cats, tree shrews, ferrets, mice, rats, and gray squirrels respectively come from Tehovnik et al. [69] (subjects: 3 macaques, unknown gender and age), Scholl et al. [50] (subjects: cats, unknown gender and age), Veit et al.[70] (subjects: 9 male and 7 female tree shrews, aged 3-8 years), Huberman et al.[71] (subjects: 8 ferrets, unknown gender and age), Niell et al.[53] (subjects: mice, aged 2–6 months, unknown gender), Foik et al.[72](subjects: 21 rats, unknown gender and age), and Hall et al.[73] (subjects: 17 gray squirrels, unknown gender and age). V1 neuron density: Neuron density data for macaques, cats, mice, rats, and gray squirrels come from Srinivasana et al.[52] (subjects: unknown gender and age); tree shrew, ferret, and gray squirrel density data respectively come from Weigand et al.[74].

Cortical magnification factor

Cortical magnification factor (CMF) data for macaques, cats, tree shrews, ferrets, mice, rats, and gray squirrels are sourced from Tehovnik et al.[69] (subjects: 3 macaques, unknown gender and age), Veit et al.[70](subjects: cats, unknown gender and age), Bosking et al.[48] (subjects: tree shrews, unknown gender and age), Rockland et al. [75] (subjects: 9 ferrets, female, unknown age), Beest et al.[54] (subjects: 28 mice, 11 males and 17 females, ages 2-14 months), Keller et al.[76] (subjects: male rats, age 3 months), and Hall et al.[73] (subjects: 17 gray squirrels, unknown gender and age).

Additionally, the anatomical data concerning inter-ocular distances are obtained from Najafian et al. [7].

A.4 Unveiling species-specific factors distinguishing pinwheels and salt-and-peppers

A.4.1 Anatomical data suggests RFs density underlying V1 organizations

Table 3: Comparative anatomical data of the retina and V1 across species.

a. Species (mean)	**b.** Retina (mm^2)	**c.** V1 size (mm^2)	**d.** V1 neurons density (neurons/mm^2)	**e.** V1 RF size in area centralis (deg)	**f.** RFD $((c) \times (d)/(b))$ (RFs/mm^2)
Macaque	636[6]	1,090[33]	243,000[33]	0.2[52]	416,462.26
Cat	510[6]	380[6, 33]	99,200[33]	1.0[50]	73,913.73
Tree shrew	122[6, 77]	73[6, 33]	192,800[74]	2.0[70]	115,363.93
Ferret	83[6, 75]	78[33]	95,813[74]	3.0[71]	90,041.13
Mouse	15[6]	2.5[33]	86,600[33]	4.0[53]	14,433.33
Rat	52[6, 78]	7.1[33]	90,800[33]	3.0[72]	12,397.69
Gray squirrel	205[6]	32[6]	84,213[74]	2.0[73]	13,145.44

We analyzed anatomical data from seven species, including primates (e.g., macaques) and non-primates (e.g., mice, rats, cats, tree shrews, gray squirrels, and ferrets), as detailed in Table 3. We first find that V1 RFs density (RFD) (ρ_{RF}) acts as a linear classifier ($y = 4.42 \times 10^4 x$), effectively distinguishing species with pinwheel structures from those with salt-and-pepper organizations. In this classifier, species like macaques, cats, tree shrews, and ferrets, which have higher RFD, are

17
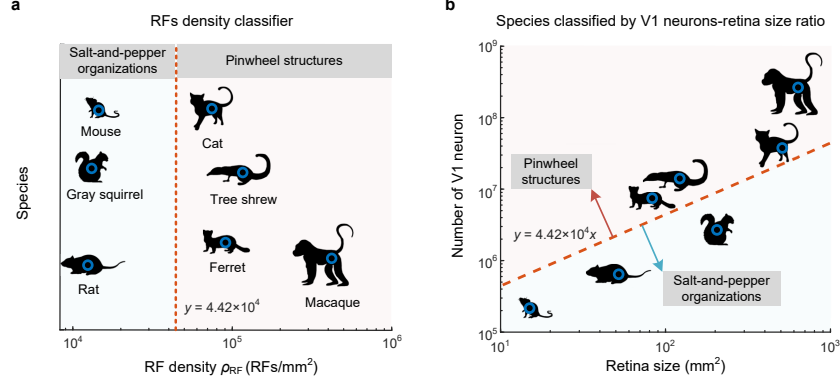
Figure 6: A linear classifier based on RFD ($y = 4.42 \times 10^4 x$) effectively differentiates species with salt-and-pepper organizations (rats, mice, gray squirrels) from those with pinwheel structures (macaques, ferrets, cats, tree shrews). **a**. This classifier reflects variations in V1 organizations across species. **b**. A plot categorizing species by the ratio of V1 neuron number to retina size acts as a divider, implying a critical ratio for the formation of pinwheel structures.

associated with pinwheel structures (light red area in Fig. 6) and exceed the classification threshold. In contrast, species with lower RFD, such as mice, rats, and gray squirrels, are linked to salt-and-pepper organizations (light blue area in Fig. 6). Thus, V1 RFD serves as a predictive metric for V1 organizational patterns across species. The ρ_{RF} is calculated as follows:

$$\rho_{RF} = \frac{n'}{s'_r} \propto \frac{n}{\left[(s_{RF} - \varepsilon)(\sqrt{n} - 1) + s_{RF}\right]^2}, \tag{12}$$

where n' denotes the total number of neurons in V1, s'_r indicates the retinal surface area. We have $n' = s_{V1} \times \rho_{V1}$, where s_{V1} corresponds to the V1 2D surface area, and ρ_{V1} signifies the neuronal density within V1. The variable ε quantifies the degree of visual input overlap among adjacent neurons, n denotes the total number of neurons, and s_{RF} represents the RF size in the self-evolving spiking neural network (SESNN). Referring to Eq. 12 and anatomical data (Table 3), the overlap ε positively correlates to V1 RFD ρ_{RF} and is a main factor influencing V1 RFD. We discuss the overlap as the variable of V1 organizations in the main text.

A.4.2 SESNN reveals neuronal connection range influencing V1 clusters

The anatomical data in Table 3d for seven species show variability in V1 neuronal density (ρ_{V1}), which influences inter-neuronal spacing and connection strength. We explore how V1 cortical orientation patterns form by adjusting the lateral connection range, impacting axon reach among E- and I-neurons, as depicted in Fig. 7. We modulate axonal arborization through parameter σ to adjust the connection range, allowing us to simulate neuronal connections in areas with varying densities. This setup enables the SESNN model to predict changes in cortical patterns (Fig. 7). Our observations indicate that increasing axon lengths, thereby extending the connection range, enlarges hypercolumn sizes within pinwheel structures (Fig. 7d), reduces the overall number of pinwheels (Fig. 7b), and increases the nearest-neighbor pinwheel distance (NNPD) (Fig. 7c). These findings underscore the critical role of neural synaptic connection range in organizing orientation maps.

A.5 Relationship between maximum values of local pixel entropy and local geometrical entropy for various shapes

To address the limitations of using local pixel entropy (LPE) with sliding windows alone to capture complex geometric properties, we conduct a new analysis comparing the maximum values of LPE with local geometrical entropy (LGE) across various shapes. These shapes include lines, angles, and junctions (L-, T-, X-junctions), as well as jagged edges. Both LPE and LGE values were normalized to the range [0,1] for consistency.

Let $P = \{v_1, v_2, \ldots, v_n\}$ be a polygon with vertices $v_i = (x_i, y_i)$, where $i = 1, 2, \ldots, n$. The edges of the polygon are the line segments between consecutive vertices, denoted as $e_i = \|v_{i+1} - v_i\|$,

18
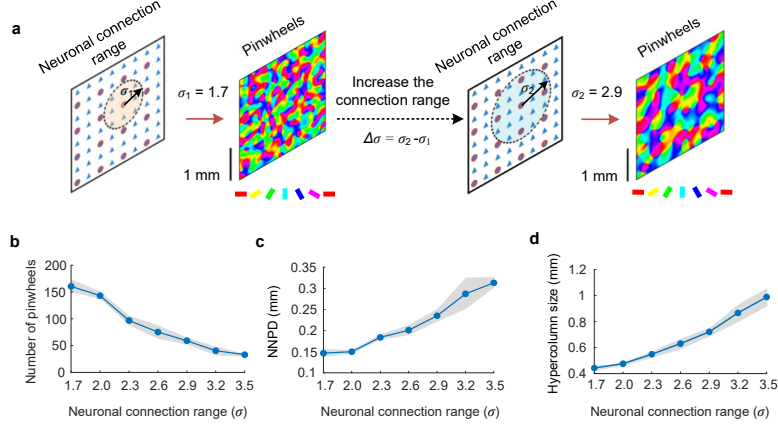
Figure 7: Neuronal connection range within V1 contributes to the formation of pinwheel structures. **a**. Modifying the synaptic connection range reshapes the dimensions of pinwheel structures. **b-d**. The relationship between the synaptic connection range (σ) and the number of pinwheels, NNPD (mm), and hypercolumn size (mm). The scale bar: 1 mm in V1 cortical surface. Color scheme: orientation preference. Lines: mean. Shaded area: SD.

where $\|\cdot\|$ represents the Euclidean distance. The angle θ_i between two consecutive edges e_i and e_{i+1} can be computed using the dot product:

$$\theta_i = \cos^{-1}\left(\frac{e_i \cdot e_{i+1}}{\|e_i\|\|e_{i+1}\|}\right). \tag{13}$$

With the set of edge lengths $\{e_1, e_2, \ldots, e_n\}$ and angles $\{\theta_1, \theta_2, \ldots, \theta_n\}$, we calculate the entropy for both distributions. The entropy H of a discrete distribution X with probability mass function $p(x)$ is given by:

$$H(X) = -\sum_{x \in X} p(x) \log p(x). \tag{14}$$

For the edge lengths and angles, the probability mass function is estimated by normalizing the frequency of occurrence of each unique edge length and angle in the polygon:

$$H(\text{Lengths}) = -\sum_{i=1}^{n} p(e_i) \log p(e_i), \tag{15}$$

$$H(\text{Angles}) = -\sum_{i=1}^{n} p(\theta_i) \log p(\theta_i). \tag{16}$$

To enhance the sensitivity of geometrical entropy to structural complexity, particularly in differentiating shapes that have similar edge lengths and angles but different structural arrangements, we introduce a scaling factor based on the logarithm of the number of vertices n. The defined geometrical entropy (GE) with the scaling factor is thus defined as:

$$GE = (H(\text{Lengths}) + H(\text{Angles})) \times \log(n). \tag{17}$$

19

This modification allows GE to capture additional complexity arising from intersections and the global arrangement of vertices, providing a more comprehensive assessment of the shape's structural intricacies.

Our results, summarized in Table 4, show that while LPE can reflect the complexity of certain patterns, it does not fully capture the geometric variations seen in more intricate shapes. For instance, the LPE values for line structures remain relatively low compared to those for jagged edges, which have the highest LPE and LGE values due to their high structural complexity. This comparison highlights the added value of incorporating LGE to better characterize local geometric structures, providing a more nuanced measure of complexity that includes both intensity distribution and spatial organization.

Table 4: Relationship between maximum values of LPE and LGE for various shapes. Both metrics are normalized to the range [0,1].

Various shapes	Max local pixel entropy	Max local geometrical entropy
Line 1	0.56	0.43
Line 2	0.56	0.43
Angle 1	0.81	0.87
Angle 2	0.79	0.86
Angle 3	0.77	0.87
L-junction	0.78	0.74
T-junction	0.78	0.64
X-junction	0.78	0.84
Jagged edges	1.00	1.00

A.6 Pinwheel centers response to different orientation bandwidths
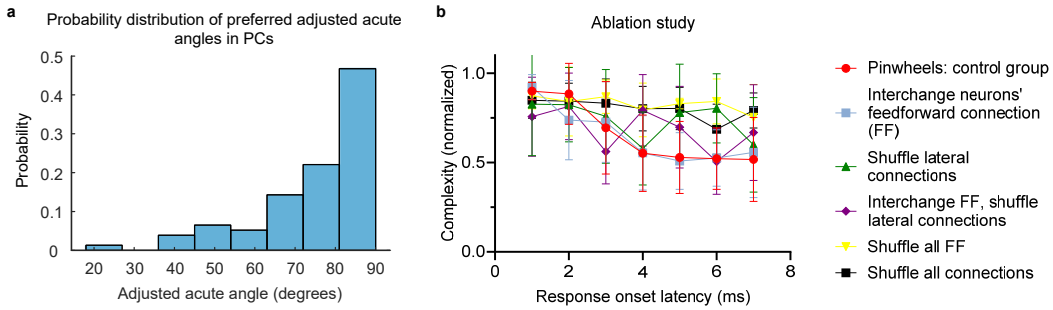
Figure 8: PCs in V1 prefer orientations and ablation study. **a**. Probability distribution of preferred acute angles in PCs. **b**. Ablation study on normalized complexity across response onset latencies. Data: mean ± SD.

Understanding the tuning of pinwheel centers (PCs) in V1 to edges, corners, and junctions is essential. In Fig. 4e, we show that PCs exhibit broader orientation tuning curves than IODs when using star-like patterns as stimuli, potentially enabling the detection of T-junctions and corners, as demonstrated by Li et al. [13] and Koch et al. [12]. We further examine the distribution of PCs' tuning curves using gratings as inputs, specifically analyzing acute angles formed by the primary and secondary peaks (Fig. 8a). This analysis reveals that PCs are more frequently associated with larger acute angles, closer to orthogonal (90°), suggesting a preference for orthogonal junctions. However, this result does not differentiate between L- and T- junctions based solely on angle. We propose that such high-order feature extraction be deferred to higher visual cortices, like V2 and V4, which are involved in texture detection, as noted by Wang et al. [79] and Roe et al. [80].

A.7 Ablation study

We present a mechanism of multiple orientation tuning that is essential for processing complexity. Our analysis of PCs' preferred acute angles (Fig. 8a) suggests that their broad tuning enables the detection

20

of complex junctions, such as T- and L-junctions, likely due to variations in local connectivity within and between iso-orientation domains.

To test this, we conduct an ablation study by disrupting local connectivity and shuffling the spatial arrangement of orientation-tuned RFs in the pinwheel orientation map, while keeping other properties constant (Fig. 8b). The control group (red) maintains higher complexity over time, whereas shuffling connections—especially both feed-forward and lateral—resulted in a decline in complexity. This highlights the importance of structured connectivity in preserving complex neural responses in V1 and supports the conclusion that structured connectivity underlies enhanced saliency detection by pinwheels.

A.8 Computing infrastructure

Table 5: Computing infrastructure

CPU	Intel® Xeon® Gold 6348 CPU @ 2.60GHz
GPU	A100
Memory	512 GB
Operating system	Ubuntu 20.04.6 LTS
Simulation platform	MATLAB R2023a and Python 3.9

The simulations and analyses in this study are performed on a high-performance computing infrastructure to ensure efficient processing of large datasets and complex models. The system is powered by an Intel® Xeon® Gold 6348 CPU running at 2.60 GHz and an NVIDIA A100 GPU, providing robust computational power for intensive tasks. The system includes 512 GB of memory, which supports handling memory-intensive applications and large-scale simulations. The operating system used is Ubuntu 20.04.6 LTS, known for its stability and compatibility with scientific software. The simulations are conducted using MATLAB R2023a and Python 3.9, both of which are widely used in scientific computing and neural modeling, enabling effective implementation and analysis of the models presented in this study.

21